Impedance Spectra and Surface Coverages Simulated Directly from the Electrochemical Reaction Mechanism:

A Nonlinear State-Space Approach

Kiran George, [†] *Matthijs van Berkel,* [‡,§,ǁ] *Xueqing Zhang,* [†] *Rochan Sinha* [†]

and Anja Bieberle-Hütter[*,†]

[†] Dutch Institute for Fundamental Energy Research (DIFFER), Electrochemical Materials and Interfaces, PO Box 6336, 5600 HH Eindhoven, The Netherlands.

[‡] Dutch Institute for Fundamental Energy Research (DIFFER), Integrated Modelling & Transport, PO Box 6336, 5600 HH Eindhoven, The Netherlands

Abstract

Current voltage curves and electrochemical impedance spectra (EIS) are crucial for investigating the performance and the electrochemical limitations of electrochemical cells. Therefore, we developed an approach which allows the direct simulation of such data based on micro-kinetic modelling. This approach allows us to assess the influence of various input parameters on the EIS and on the current-voltage curves and, hence, the overall performance of electrochemical cells. We develop our approach for the oxygen evolution reaction (OER) taking place at the semiconductor-electrolyte interface. At this interface the micro-kinetic equations, i.e., electrochemical reactions, for the multiple steps in OER are formulated and the resulting

set of equations are modeled in a state-space form. As input to the state-space model we use the theoretical reaction rates calculated using density functional theory and Gerischer theory for semiconductors. Then, the electrochemical data is simulated as a function of applied potential. Next to the theory and the model development, a case study on the hematite-electrolyte interface which is a typical interface in photo-electrochemical cells, is presented. Current voltage curves and EIS data for the hematite interface are simulated from the electrochemical model. The data is compared to experimental measurements. Apart from the current density and the EIS, the model can simulate the coverage of intermediate species as a function of applied potential which is highly demanded for identifying the limiting processes at the interface, but not available from experimental studies. The approach is generic and can be used for other electrochemical interfaces, such as present in fuel cells, electrolysers, or batteries.

1. Introduction

Solar energy conversion technologies will play a crucial role in satisfying the global demand for clean and sustainable energy. In particular, conversion of solar energy into chemical energy is a promising path.[1] Photo-electrochemical cells (PEC) are a possible solution to perform this conversion.[2] Due to the intermittent nature of solar irradiation, cost-effective storage of energy is very important for solar energy conversion devices. PECs have an advantage here compared to other solutions as they convert solar energy directly into storable fuels.[3,4] However, the conversion efficiencies of PECs using earth abundant materials need to be significantly improved such that they can be commercialized. This calls for specific research towards identifying the limiting processes at the electrochemical interface and improving their efficiency.

In a PEC, water is split into hydrogen and oxygen at its electrodes using solar energy. The anode of a PEC is generally made of a semiconductor material (binary metal oxides, such as

TiO_2,[5] Fe_2O_3,[6] WO_3 [7] or complex metal oxides, such as $BiVO_4$ [8]) which generates electron-hole pairs under illumination. The holes move towards the semiconductor-electrolyte interface, where they oxidize the water to form oxygen. This is called the oxygen evolution reaction (OER). Meanwhile, the electrons move to the back contact and further to the counter electrode where they reduce water to form hydrogen (hydrogen evolution reaction, HER). Of these two half reactions, the OER is a more complex process since it requires the transfer of four electrons.[9] This exchange of electrons takes place in several steps and results in various intermediate species.

Several experimental and theoretical approaches are proposed in the literature to improve our understanding of PEC in view of identifying the processes that limit the performance of PECs.[10,11] These processes consist of a combination of thermodynamics, semiconductor properties, and reaction kinetics.

The thermodynamics of the intermediate species are mostly studied in theory using density functional theory (DFT) by calculating the free energies of formation of intermediates and the overpotentials.[12–16] Additionally, DFT is used for calculating semiconductor properties, like bandgaps, band edge positions[17,18], as well as the effect of doping, vacancies, or surface orientation on the OER overpotential.[19–21] The reaction kinetics of solid-water interfaces are studied by molecular dynamics (MD)[22–24] simulations. These theoretical approaches have helped in understanding the behavior of electrode materials at atomistic and molecular scale. A recent review by Zhang et al.[25] summarizes the different approaches and results.

Experimentally, PEC interfaces are in first instance characterized by current-voltage curves, which allow for direct assessment of the overpotential. The overpotential is determined by the thermodynamics, semiconductor properties, and the kinetics at the interface. The kinetics of processes happening at the electrodes are studied by analyzing electrochemical impedance spectra (EIS)[26,27] at single operating points. The measured EIS data is usually fitted to electrical

circuits consisting of resistances, capacitances, and inductances, which are called the equivalent circuit models.[28] These equivalent circuit elements are attributed to physical and chemical processes at the electrochemical interface, such as the electrical double layer, charge transfer reactions, space-charge layer, and external circuit contacts.[29,30] However, there exists no direct relation between the electrical quantities and physical and chemical processes at the interface; the connection to individual reaction steps and intermediate species is missing.

An alternative approach in theoretical study of PEC is based on analytical models [31–33] which use semiconductor properties along with a thermodynamic single step reaction for the OER. These studies allow to predict the overall performance of the cells under given operating conditions and consider the semiconductor properties, such as carrier generation, charge transport, recombination, charge transfer, band bending, and the Helmholtz layer[4,34–37]. However, as only a single step OER mechanism is considered, the full thermodynamics and kinetics of the intermediate species are not considered.

In reality, however, intermediate species are present and were also proven experimentally by methods, such as transient absorption spectroscopy (TAS)[38], Fourier transform infra-red spectroscopy (FTIR)[39,40], and transient (optical) grating spectroscopy (TGS)[41]. There is still an ongoing debate in the literature about which reaction paths are of importance[25,42], which intermediate reaction steps are rate-limiting[25], and whether intermediate species exist long enough to be observed in experiments. However, to answer these fundamental questions it is crucial to arrive at an approach that combines thermodynamics, reaction kinetics of the multi-step reactions, and semiconductor properties in a way that the outcome of such a model can be compared directly to experimental observations. Such an overall approach can only be achieved by considering the microkinetics, which has been recognized in the literature as highly necessary.[43,44] Exner et al.[45] summarized that "microkinetics is of course the missing link for critical theory/experimental comparison".

To close this gap, we propose here a new approach to model electrochemical data and to reproduce experimental data directly from theory. This approach combines DFT and microkinetics with the Gerischer model[46] of electron transfer for semiconductors. Thereby, we demonstrate for the first time that measurable quantities, such as onset potential and electrochemical impedance, can be simulated based on a pure electrochemical model. In addition, our approach allows for the calculation of the coverage of intermediate species which is currently experimentally not measurable. Semiconductor properties, such as the valence band position and hole density are included in our model and it can be studied how they affect the EIS, overpotential, and coverage of intermediate species. The model itself has been formulated as a nonlinear state-space model, which significantly simplifies the analysis and simulations due to the availability of standard tool boxes[47,48]. The model is built using electrochemical reactions derived from the literature. Different reaction mechanisms can be easily implemented which is a tremendous advantage of this approach when it comes to identifying the limitations at electrochemical interfaces using theory/experiment comparison. The schematic representation of the state-space model of our electrochemical system is shown in Figure 1.

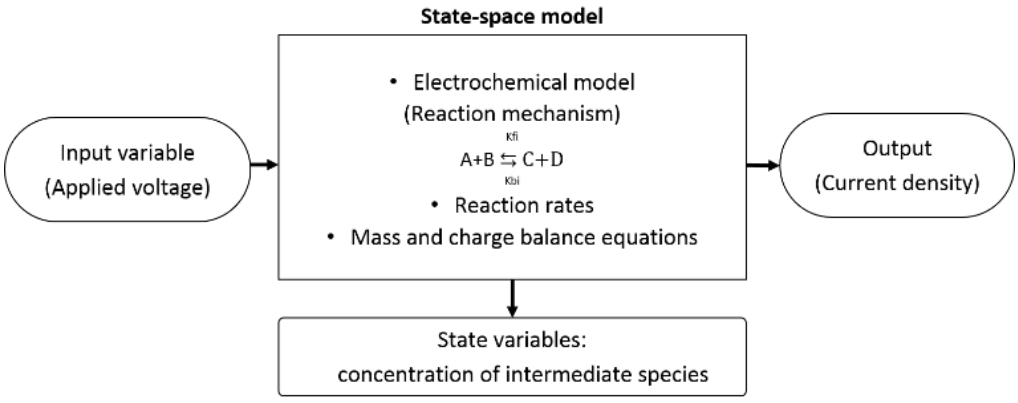

Figure 1. Representation of state-space model of an electrochemical system. The input variable is the applied voltage, the output variable is the current density, and the state variables are the concentration of intermediate species from mass balance equation.

It is important to note that this work is in part inspired by previous, preliminary microkinetic modelling studies which were carried out on metals (not on semiconductors). These include a) microkinetic simulations of multi-step Oxygen Reduction Reactions (ORR) by Hansen et al.[49]; these simulations were combined with DFT and MD simulations; b) microkinetic simulations of the cathodic and anodic reactions in solid oxide fuel cells (SOFC) by Mitterdorfer et al. [50] and Bieberle et al.[51], respectively. In addition, different methods for identifying the reaction rates have been discussed in the literature based on microkientic modeling and Butler-Volmer theory for metallic electrodes.[52–54]

In summary, the novel approach that we introduce in this study, is a bridge between first-principle calculations and experimental measurements for semiconductor electrodes. It combines thermodynamics, semiconductor properties, and reaction kinetics in one model. The model simulates quantities which are measured in experiments and allows for the calculation of experimentally not available data, such as surface coverages of intermediate species. The paper is divided in two parts: a) model and method and b) a case study on the hematite (Fe_2O_3)-water interface.

2. Model and Method

This section introduces the microkinetic model and the corresponding nonlinear state-space model. Concrete values of parameters are not given here, but will be discussed in chapter 3 with the case study of the hematite (Fe_2O_3)-water interface.

2.1 Mechanism of water oxidation

The first step in model construction is to choose the mechanism of OER. In an electrochemical cell, the electrolyte can be acidic or alkaline. Depending on the pH of the electrolyte, OER can proceed in two different ways. In acidic environment, the OER is given by[25]

$$2H_2O + 4h^+ \rightarrow O_2 + 4H^+ \qquad (1)$$

and in alkaline environment it is[55]

$$4OH^- + 4h^+ \rightarrow O_2 + 2H_2O \qquad (2)$$

These overall reactions can proceed via different multistep mechanisms. Since OER involves transfer of four electrons/holes, it has been proposed in the literature that the entire reaction consists of four single charge-transfer steps. A detailed review about different mechanisms that have been suggested in the literature can be found elsewhere.[25] In this study, reactions in an alkaline environment are considered and the mechanism proposed by Hellman et al.[56] is chosen. This mechanism is based on the multistep OER proposed earlier by Rossmeisl et al.[13] The four step electron transfer reactions in alkaline environment are

$$* + OH^- + h^+ \underset{K_{b1}}{\overset{K_{f1}}{\rightleftharpoons}} OH_{ad} \qquad (3)$$

$$OH_{ad} + OH^- + h^+ \underset{K_{b2}}{\overset{K_{f2}}{\rightleftharpoons}} O_{ad} + H_2O \qquad (4)$$

$$O_{ad} + OH^- + h^+ \underset{K_{b3}}{\overset{K_{f3}}{\rightleftharpoons}} OOH_{ad} \qquad (5)$$

$$OOH_{ad} + OH^- + h^+ \underset{K_{b4}}{\overset{Kf_4}{\rightleftharpoons}} O_{2,ad} + H_2O \qquad (6)$$

Here * represents an adsorption site and the subscript *ad* means that the species are adsorbed on the surface. Thus, OH_{ad}, O_{ad}, OOH_{ad}, and O_{2ad} are the intermediate species adsorbed on the surface during the OER. The forward and backward reaction rates of these charge transfer reactions are represented by K_{fi} and K_{bi}, respectively, where i = 1 to 4. After adsorbed oxygen ($O_{2,ad}$) is formed at the site, it desorbs ($O_{2,des}$) from the surface at a rate of K_{f5} which is given by

$$O_{2,ad} \overset{K_{f5}}{\rightarrow} O_{2,des} + * \qquad (7)$$

This step does not involve charge transfer and, hence, the desorption rate K_{f5} is chosen as a constant.

Once the mechanism is selected, the next step is to model these reactions such that the net current due to charge transfer can be calculated. In order to do this, corresponding rates of the multi-step reactions have to be known. For electron transfer reactions, rates can be calculated based on the Butler-Volmer theory, the Marcus theory,[57] or the Gerischer theory.[58] The Butler-Volmer theory uses first-order reaction rates and is best suited for reactions involving metallic electrodes.[59] This has been used in the modelling of SOFC by Mitterdorfer et al.,[60] Bieberle et al.,[51] and Hansen et al.[49] However, for modeling semiconductor interfaces, the Butler-Volmer theory is not suitable.[59] Unlike metals, in the case of semiconductors, most of the applied potential falls across the space charge layer and charge transfer occurs via the conduction band or valence band.[46] The Gerischer theory takes this into account and defines separate expressions for the charge transfer rate for electron transfer via valence band and conduction band. We therefore use the Gerischer theory in this study.

2.2 Calculation of reaction rates

An n-type semiconductor anode under reverse bias is considered for the model discussed here. Hole transfer via the valence band is believed to drive the reaction at the semiconductor-electrolyte interface. Hence, the Gerischer expression for the hole transfer via the valence band is used. For calculating charge transfer rates for each intermediate step (eq. 3 – 6), the Fermi level of the redox system in the original expression is replaced with the redox level of each intermediate species. Thus, forward and backward charge transfer rates for each intermediate step, $\overline{k_{fl}}$ and $\overline{k_{bl}}$, respectively, are calculated as[61]

$$\overline{k_{fi}} = k_{v,max} \exp\left[-\frac{\left(E_v - E^0_{F,redox,i} - \lambda\right)^2}{4k_B T\lambda}\right] \quad (8)$$

$$\overline{k_{bi}} = k_{v,max} \exp\left[-\frac{\left(E_v - E^0_{F,redox,i} + \lambda\right)^2}{4k_B T\lambda}\right] \quad (9)$$

where $k_{v,max}$ is a pre-exponential factor with the dimension [cm^4/s],[61] E_v is the energy at the upper edge of the valence band of the semiconductor, k_B is the Boltzmann constant, T is the temperature, λ represents the solvent reorganization energy,[62] and $E^0_{F,redox,i}$ is the redox potential of the i^{th} reaction.

The redox potential for each intermediate can be determined from Gibbs free energy change of formation $(\Delta G)_i$ of the corresponding intermediate species at the surface. The relation between Gibbs free energy and redox potential is given as[63]

$$\Delta G_i = nFE^0_{F,redox,i} \quad (10)$$

where n is the number of electrons transferred and F is the Faraday constant. The values of ΔG_i are material dependent and are derived from DFT calculations, such as shown in Rossmeisl et al.[13] In eq. 10, F can be omitted as these DFT calculations give ΔG_i (eV) for single electron transfer reactions.

The forward and backward current density [A cm^{-2}] are then calculated as[61]

$$j_{fi} = e\overline{k_{fi}}\, p_s c_{red,i} \quad (11)$$

$$j_{bi} = e\overline{k_{bi}} N_v c_{ox,i} \quad (12)$$

where e is the elementary charge of an electron, N_v [cm^{-3}] is the effective density of states of the valence band, p_s [cm^{-3}] represents the hole density at the surface of the semiconductor, $c_{red,i}$ and $c_{ox,i}$ are the concentrations of reduced and oxidized intermediate species [cm^{-3}],

respectively. The hole density increases exponentially as a function of applied potential u given by[61]

$$p_s = p_s^0 \exp\left(\frac{u}{K_B T}\right) \qquad (13)$$

where p_s^0 is the equilibrium hole density at the surface in the dark. The concentrations of intermediate species are calculated by solving the rate equations, which is explained in the following section.

2.3 Rate equations and charge balance relations

The reaction steps given in eq. 3-7 are used to formulate rate equations for all the intermediate species adsorbed on the semiconductor surface assuming Langmuir adsorption isotherm. These equations form a set of coupled nonlinear ordinary differential equations as listed in eq. 14 - 17.

$$\dot{\theta}_{OH} = K_{f1} x_{OH}\, \theta_{ad} - K_{b1}\theta_{OH} - K_{f2}\theta_{OH} x_{OH} + K_{b2}\theta_O x_{H_2O} \qquad (14)$$

$$\dot{\theta}_O = K_{f2} x_{OH}\, \theta_{OH} - K_{b2}\theta_O x_{H_2O} - K_{f3}\theta_O x_{OH} + K_{b3}\theta_{OOH} \qquad (15)$$

$$\dot{\theta}_{OOH} = K_{f3}\theta_O x_{OH} - K_{b3}\theta_{OOH} - K_{f4}\theta_{OOH} x_{OH} + K_{b4}\theta_{O_2} x_{H_2O} \qquad (16)$$

$$\dot{\theta}_{O_2} = K_{f4}\theta_{OOH} x_{OH} - K_{b4}\theta_{O_2} x_{H_2O} - K_{f5}\theta_{O_2} \qquad (17)$$

$$\theta_{ad} = 1 - \theta_{OH} - \theta_O - \theta_{OOH} - \theta_{O_2} \qquad (18)$$

where θ_{ad} is a dimensionless quantity representing the fraction of free adsorption sites. The value of θ_{ad} ranges between 0 and 1. All other θ_i are the fractional coverages of intermediate species i, where i represents OH, O, OOH, and O_2. The terms x_{OH} and x_{H_2O} are the mole fractions of hydroxyl ions and water in the bulk electrolyte, respectively. In eq. 14 – 17, K_{fi} and K_{bi} are defined as

$$K_{fi} = \overline{k_{fi}} p_s \quad (19)$$

$$K_{bi} = \overline{k_{bi}} N_v \quad (20)$$

The concentration is defined as the number of intermediate species adsorbed per site which, by eq. 3 - 6, relates to the number of holes transferred. Thus, the model uses fractional concentration of species per unit site. However, the current density is the collective hole transfer rate from the multi-step reactions at each site on the surface. Thus, the number of adsorption sites (N_0) available at the electrode surface is necessary for the calculation of the total current density. The current balance equations in eq. 11 - 12 become

$$j_f = eN_0\left(K_{f1}\theta_{ad} + K_{f2}\theta_{OH} + K_{f3}\theta_O + K_{f4}\theta_{OOH}\right)x_{OH} \quad (21)$$

$$j_b = eN_0\left(K_{b1}\theta_{OH} + K_{b2}\theta_O x_{H_2O} + K_{b3}\theta_{OOH} + K_{b4}\theta_{O_2} x_{H_2O}\right) \quad (22)$$

$$j = j_f - j_b \quad (23)$$

where j [A cm^{-2}] is the total current density and N_0 is the density of adsorption sites at the semiconductor surface [cm^{-3}]. The rate equations and charge balance relations are then modeled in a state-space form.

2.4 State-space model

The rate equations and charge balance relations can be formulated in a general nonlinear state-space model, which results in [64 65]

$$\frac{d\Theta(t)}{dt} = f\left(\Theta(t), u(t)\right) \quad (24)$$

$$\boldsymbol{J}(t) = g\left(\Theta(t), u(t)\right) \quad (25)$$

Here, eq. 24 is called the state equation and eq. 25 the output equation. In these equations, Θ represents the set of state variables, u is the input variable and $\boldsymbol{J}(t)$ is the output vector. Together eq. 24 and eq. 25 form the general form of a state-space model. Comparing this general form to the mass and charge balance equations (eq. 14 - 18 and eq. 21 - 23), it can be seen that this set of equations forms a state-space model.

The fractional concentrations of intermediate species, θ_{OH}, $\theta_O, \theta_{OOH}, and\ \theta_{O_2}$ are the state variables (Θ) and the current density j is the output ($\boldsymbol{J}$). The concentration of adsorbed species and current density vary with applied potential u, which is the input variable in this system. The resulting model is a single input (applied voltage) - single output (current density) model with four state variables (concentrations of four intermediate species). The state-space model is implemented using MATLAB/Simulink[66] and the resulting model is a nonlinear state-space model. It is nonlinear because the carrier density at the surface varies exponentially with applied potential. The set of equations are solved along with the site conservations constraint given in eq. 18. From the solution, the coverage of different intermediate species can be calculated for any applied potential.

2.5 Linearization of state space model and impedance calculation

The state-space model can be used to simulate impedance spectra at different potentials similar to experiments. In order to calculate the impedance, the model has to be linearized around the chosen operating point.[64] The reaction rates in the model are written in the expanded form using eq. 13, 19 and 20. The input variable, state variables and output are defined as

$$u = u_{eq} + \tilde{u} \tag{26}$$

$$\Theta = \Theta_{eq} + \tilde{\Theta} \tag{27}$$

$$\boldsymbol{J} = \boldsymbol{J_{eq}} + \tilde{\boldsymbol{J}} \tag{28}$$

Here, u_{eq} represents any equilibrium potential, Θ_{eq} represents the state variables at this potential, and $\boldsymbol{J_{eq}}$ represents the corresponding output. The added terms, $\tilde{u}$, $\widetilde{\Theta}$ and $\tilde{\boldsymbol{J}}$ represent the perturbation of the respective variables around equilibrium. The perturbation of state variable $\widetilde{\Theta}$ is a vector given by

$$\widetilde{\Theta} = \begin{bmatrix} \tilde{\theta}_{OH} & \tilde{\theta}_{O} & \tilde{\theta}_{OOH} & \tilde{\theta}_{O_2} \end{bmatrix}^T \tag{29}$$

The linearization is calculated using a Taylor series expansion of eq. 24 and eq. 25 which is truncated after the first order derivatives. Thus, assuming $\tilde{u}$ and corresponding responses $\widetilde{\Theta}$ and $\tilde{\boldsymbol{J}}$ to be small, the linearized model around the equilibrium point is obtained as

$$\frac{d\widetilde{\Theta}}{dt} = A\widetilde{\Theta} + B\tilde{u} \tag{30}$$

$$\tilde{\boldsymbol{J}} = C\widetilde{\Theta} + D\tilde{u} \tag{31}$$

where,

$$A = \left.\frac{\partial f}{\partial \Theta}\right|_{u_{eq},\Theta_{eq}} \quad B = \left.\frac{\partial f}{\partial u}\right|_{u_{eq},\Theta_{eq}}$$

$$C = \left.\frac{\partial g}{\partial \Theta}\right|_{u_{eq},\Theta_{eq}} \quad D = \left.\frac{\partial g}{\partial u}\right|_{u_{eq},\Theta_{eq}} \tag{32}$$

The expressions for A, B, C and D are listed in Table. 1. In order to simplify these expressions, we define the term

$$U_{eq} = {p_s}^0 \, exp\left(\frac{u_{eq}}{k_B T}\right) \tag{33}$$

Table 1. Expressions for matrix coefficients from linearization in terms of intermediate reaction rates.

$$A = \begin{bmatrix} -U_{eq}\left(\overline{k_{f1}} + \overline{k_{f2}}\right)x_{OH} - N_v\overline{k_{b1}} & N_v\overline{k_{b2}}\, xH_2O - U_{eq}\overline{k_{f1}}\, x_{OH} & -U_{eq}\overline{k_{f1}}x_{OH} & -U_{eq}\overline{k_{f1}}x_{OH} \\ U_{eq}\overline{k_{f2}}x_{OH} & -N_v\overline{k_{b2}}\, xH_2O\ - U_{eq}\overline{k_{f3}}x_{OH} & N_v\overline{k_{b3}} & 0 \\ 0 & U_{eq}\overline{k_{f3}}x_{OH} & -N_v\overline{k_{b3}} - U_{eq}\overline{k_{f4}}x_{OH} & N_v\overline{k_{b4}}\, x_{H_2O} \\ 0 & 0 & U_{eq}\overline{k_{f4}}x_{OH} & -K_{f5} - N_v\overline{k_{b4}}x_{H_2O} \end{bmatrix}$$

$$B = \frac{U_{eq}}{k_B T}\begin{bmatrix} \left(\overline{k_{f1}}x_{OH}\theta_s^{eq} - \overline{k_{f2}}x_{OH}\theta_{OH}^{eq}\right) \\ \left(\overline{k_{f2}}x_{OH}\theta_{OH}^{eq} - \overline{k_{f3}}x_{OH}\theta_O^{eq}\right) \\ \left(\overline{k_{f3}}x_{OH}\theta_O^{eq} - \overline{k_{f4}}x_{OH}\theta_{OOH}^{eq}\right) \\ \left(\overline{k_{f4}}x_{OH}\theta_{OOH}^{eq}\right) \end{bmatrix}^T$$

$$C = N_0\, q_e\begin{bmatrix} -\overline{k_{b1}}N_v + \left(-\overline{k_{f1}} + \overline{k_{f2}}\right)U_{eq}x_{OH} \\ -\overline{k_{b2}}xH_2ON_v + \left(-\overline{k_{f1}} + \overline{k_{f3}}\right)U_{eq}x_{OH} \\ -\overline{k_{b3}}N_v + \left(-\overline{k_{f1}} + \overline{k_{f4}}\right)\, U_{eq}\, x_{OH} \\ -\overline{k_{b4}}xH_2ON_v - \overline{k_{f1}}U_{eq}x_{OH} \end{bmatrix}^T$$

$$D = \frac{U_{eq}N_0 q_e x_{OH}}{k_B T}\left[\overline{k_{f1}}\theta_s^{eq} + \overline{k_{f2}}\theta_{OH}^{eq} + \overline{k_{f3}}\theta_O^{eq} + \overline{k_{f4}}\theta_{OOH}^{eq}\right]$$

For calculating the impedance spectra, an input-output relation in the frequency domain has to be derived. This is done by applying Laplace transform ($\mathcal{L}$) on eq. 30 and eq. 31 and solving the resulting equations to get a relation between output and input variable given by[48]

$$\frac{\tilde{\boldsymbol{J}}(s)}{\tilde{u}(s)} = H(s) = C(sI - A)^{-1}B + D \qquad (34)$$

where s represents the Laplace variable. $H(s)$ is measurable only on the imaginary axis. Hence, we consider $s = i\omega$, where $i = \sqrt{-1}$ and ω is the frequency of perturbation on the input variable.[67] $\tilde{\boldsymbol{J}}(s)$ and $\tilde{u}(s)$ represent the Laplace transform of output and input variable, respectively. $H(s)$ is called the transfer function matrix and in this case it represents admittance

$Y(s)$ of the system. The impedance $Z(s)$ is defined as the reciprocal of admittance $Y(s)$ given by

$$Z(s) = Y(s)^{-1} = H(s)^{-1} \qquad (35)$$

This expression allows generating impedance spectra directly from electrochemical equations which is a novelty for PEC interfaces and electrochemical interfaces in general.

3. Case study: Hematite (Fe_2O_3) – water interface

In this section, we demonstrate the implementation of the developed model for hematite (Fe_2O_3)-water interface. Hematite is a widely studied photoanode material because of its abundance, low cost, and non-toxicity.[6,68,69] Hematite is stable over a wide pH-range and has a suitable band gap (2.1 eV) for water oxidation under visible light.[70,71] Theoretically, PEC cells made with hematite photoanodes can reach an efficiency of 15%,[68] which along with the above mentioned factors make hematite a suitable material for PEC anodes. However, under experimental conditions, hematite shows lower efficiency compared to the theoretical predictions, most likely due to sluggish reaction kinetics at the hematite-water interface and due to the short hole diffusion length (2-4 nm).[6] It is therefore of utmost interest to understand the limitations at the (Fe_2O_3)-water interface. The implementation of the hematite-water interface in this chapter is done by substituting hematite-specific parameters into the model that was developed in chapter 2. The hematite (110) surface is used in this study, since this surface has been observed to be the most active surface according to both theoretical[14] and experimental studies.[72]

In experimental studies, measurements are done in both dark and illuminated conditions.[73,74] The OER mechanism remains the same irrespective of whether the reactions are taking place under illumination or in the dark. Regarding the kinetics at the interface, mainly the number of electron-hole pairs increase during illumination. Hence, the model itself does not change and

can be used for simulation of electrochemical data under illumination and in dark conditions. However, for simulating EIS under illumination the effects of light on the semiconductor bulk also has to be taken into account. This needs further analysis and is therefore planned for the future.

3.1 Input parameters

There are different material dependent and system dependent parameters needed for the calculation of the reaction rates. The parameters used in the model are listed in Table. 2.

Table 2. Description of parameters used in the model with values used for simulating hematite-water interface.

Parameter	Description	Value
$k_{v,max}$	Rate constant pre-exponential factor for valence band hole transfer	10^{-16} $cm^4 s^{-1}$ [75]
N_v	Density of energy states at the upper edge of the valence band	10^{22} cm^{-3} [76]
λ	Solvent reorganization energy	1 eV [46,77]
E_v	Upper edge of valence band vs NHE	2.4 V [68]
$E^0_{F,redox}$	Redox potential of the species involved	from DFT calculation
u	Applied potential	0 - 1.8 V vs RHE
N_0	Number of adsorption sites calculated for hematite (110) surface	2.43x 10^{15} cm^{-3}
pH	pH of the solution	13.8
T	Temperature	298 K
K_{f5}	Rate of desorption	10^8 s^{-1} [49]

The concentration of OH^- ions in the electrolyte solution is calculated from the pH-value of 13.8 that is used in experiments. In order to investigate the reaction kinetics and to calculate the

redox potential for each intermediate (eq. 10), we use the Gibbs free energies calculated by Zhang et al.[14] on Fe_2O_3 (110) surface (Table 3). These DFT calculations were done for the solid-gas interface and do not consider the solid-liquid interface present in the experiments. In addition, the Gibbs free energies from DFT are calculated for the case of zero bias potential at the surface. For any applied bias at the interface, a correction has to be made by subtracting the bias potential value from the DFT calculated value.[13] At the electrode-electrolyte interface, there is a bias due to potential drop across the Helmholtz layer.[78] Thus, to accommodate this, the value of the Helmholtz potential is subtracted from the free energy values in Table 3 in the model.

Table 3. DFT calculated Gibbs free energies for reaction intermediates in OER steps on Fe_2O_3 (110) surface used for calculating reaction rates.[14]

OER Step	ΔG (eV)
OH adsorption	1.461
O adsorption	2.011
OOH adsorption	1.204
O_2 adsorption	0.239

Note that the reaction rates do not change with pH, since the band positions and redox potentials shift to the same extent with change in pH.[2] The number of adsorption sites (N_0) is obtained from the geometry of hematite (110) surface used for DFT analysis. This is done by calculating the number of atoms present per unit area of the optimized hematite surface. We consider all the atoms on the Fe_2O_3 surface to act as adsorption sites for reaction intermediates. Experimental electrodes usually do not have a flat surface. Due to surface roughness, the density of adsorption sites per unit geometric area of the electrode is larger than that of the flat surface. In order to accommodate the surface roughness in the simulations, the density of active sites on the surface (N_0) calculated from flat surface is multiplied by a constant factor. A multiplication factor of 5 is used for the simulations in this case study. The hole density at the surface at

equilibrium in the dark, p_s^0, is calculated using carrier density equations for doped semiconductors.[79]

3.2 Assumptions

For this case study, we use the following assumptions:

- All reactions are considered to take place in the dark and the reactions proceed with the application of an external potential.
- Any change in applied potential falls across the electrode only and the potential drop across the Helmholtz layer (V_H) remains constant.[2]
- The pH of the solution and the temperature remain constant during the reaction.
- For calculating the reaction rates, pre-exponential factor ($k_{v,max}$) and solvent reorganization energy (λ) are assumed to be same for all the steps in OER.

DFT calculations are based on the solid-gas interface and do not consider the solid-liquid interface which is the real interface in experiments.

3.3 Simulated data from the electrochemical model

In this section, we show the calculation of current–voltage characteristics, coverage plots, and impedance spectra from the developed electrochemical model.

3.3.1 Current-voltage characteristic

A linearly varying potential u from 0 to 1.8 V is chosen as input to the model. The current density plot is obtained by plotting the output of the model (j) against the applied potential. For the simulation results to be similar to the experiments, the series resistance (R_s) associated with the back contact, which leads to a potential drop, needs to be considered. The potential drop associated with this series resistance is $j.R_s$. Hence, for an applied potential of u, the effective

potential available across the semiconductor-electrolyte interface will be $u - j.R_s$. This potential drop is accommodated in the model and for the simulations in this study, an R_s value of 30 Ohms is used. The calculated current density is plotted against the applied input potential u in Figure 2a. The plot shows an onset potential of around 1.7 V. The current density plot from the model qualitatively compares well with the experimental dark current measurements in literature.[73,80] We need to note that simulation results in Figure 2a (current density and onset potential) depend on the reaction rates and input parameters in Table 2 which are derived from DFT calculations and literature. For example, if a higher surface hole density (p_s^0) is chosen, the onset will take place at a lower applied potential. This trend is similar to experimental results under illumination, as surface hole density is higher under illumination, the onset will be at lower potentials.

3.3.2 Species coverage plot

Unlike the current-voltage characteristic, which is experimentally measurable, the coverage of intermediate species cannot be obtained from measurements straightforwardly. However, with our model we can calculate the coverage of intermediate species at the surface based on the theoretical reaction rates. Figure 2b shows the fractional coverage of intermediate species adsorbed on hematite as a function of applied potential. Up to an applied voltage of about 1.3 V, θ is 1 which means that all adsorption sites are free. At potentials higher than 1.3 V, adsorbed OH increases and θ decreases. Between 1.5 V and 1.7 V, OH is the only species adsorbed at the surface. At potentials higher than 1.7 V all the other intermediates O, OOH, and O_2 are formed. The adsorbed O and O_2 are not visible in this plot, since the coverages are relatively small. This coverage plot is based on the theoretical reaction rates and the input values used in the model. It proves that once the model is established, trends for the surface coverages can

easily be calculated which delivers data which is extremely challenging to obtain experimentally. In particular, surface coverages can be scanned for different input values for the electrochemical interface and for different electrochemical models. The trends of surface

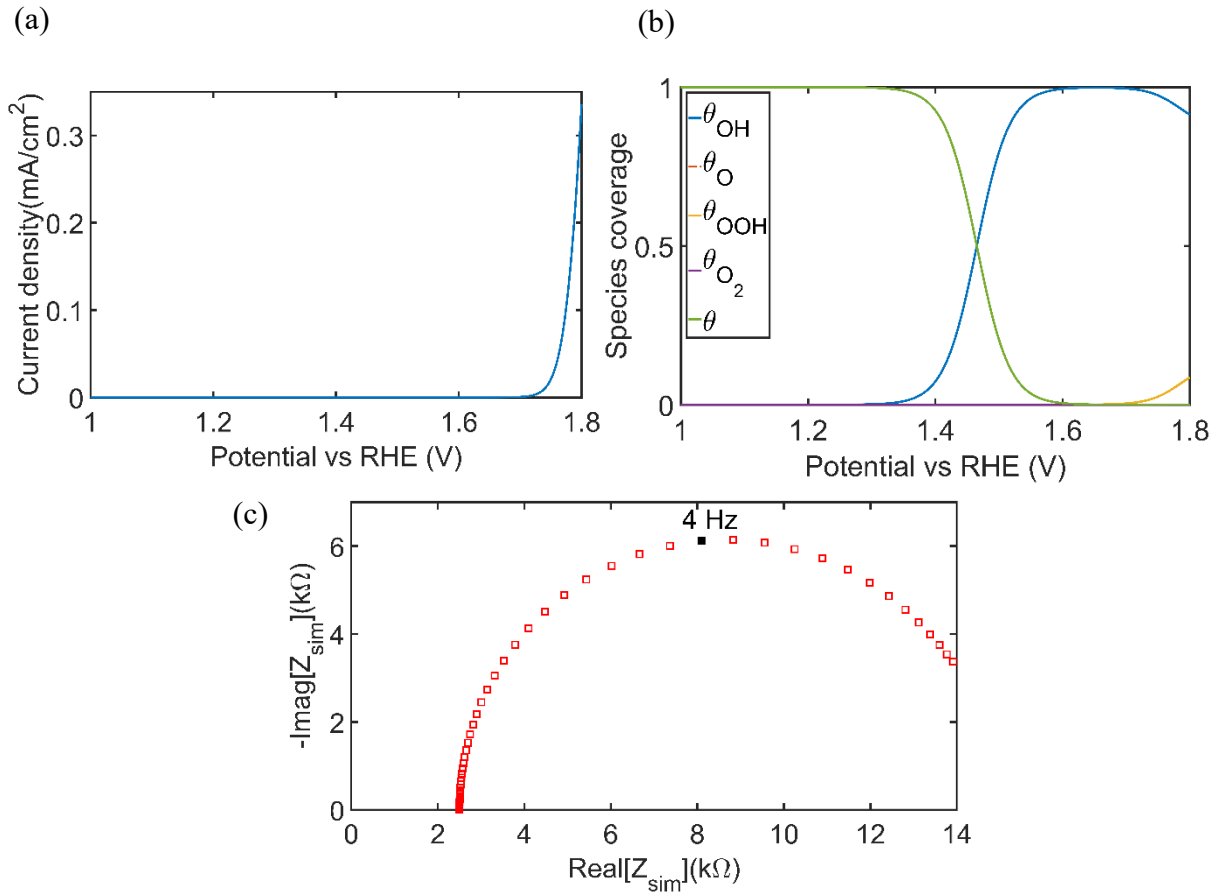

Figure 2. (a) Current- voltage characteristic plotted using the nonlinear state-space model. The onset potential is around 1.7 V which is close to the experimentally observed value. The onset potential depends on the reaction rates and the input parameters; (b) Surface coverages of intermediate species adsorbed on the hematite surface as a function of applied potential. θ is the fractional ratio of free adsorption sites available and θ_i is the fractional coverage of intermediate species i. The concentration of species O (θ_O) and O_2 (θ_{O_2}) are not visible as the coverage is small compared to the other species; (c) Impedance spectrum calculated at 1.7 V from the linearized state-space model. This impedance spectrum represents the impedance from interface reactions at 1.7 V, according to the rates calculated using Gerischer model, for the frequency range of 0.8 Hz to 30 kHz.

coverages as a function of applied potential give novel insight into the kinetics at the interface. Once the model parameters are optimized with experimental data, quantitative data can be obtained as well.

3.3.3 Electrochemical Impedance Spectrum (EIS)

Impedance spectra are calculated at different applied potentials by linearization of the model at the specific potentials, as explained in section 2.5. Technically, EIS can be calculated for any applied potential. The calculation requires corresponding equilibrium values of state variables at that potential, i.e. fractional coverage of intermediate species, as derived in section 2.5. For this, first the potential for which the impedance spectrum is calculated, is given as a constant input to the nonlinear model. Then, the steady state values of all the state variables in equilibrium at this applied potential are calculated. These equilibrium values of the state variables and the potential are substituted in the linearized model to calculate the impedance spectrum at that specific potential. A representative EIS at a potential of 1.7 V (just before the onset potential) is shown in Figure 2c in the frequency range of 0.8 Hz to 30 kHz. This spectrum represents the impedance only from charge transfer reactions at the electrode-electrolyte interface based on the assumed mechanism of OER (eq. 3-6). It does not consider other contributions, like impedance related to external circuit, semiconductor bulk, trapping/de-trapping resistance of hole transfer from valence band, which are part of experimental spectra. Hence, for the comparison of simulated impedance from the model to the experiments, other impedance contributions have to be added to the charge transfer impedance part; this is discussed in section 3.5.

3.4 Model order reduction

Model order reduction is a technique that allows to simplify a model based on the behavior of a system and the order of the transfer function of the model. We want to show in this section,

how model order reduction can be used to simplify the charge transfer reaction model to determine reaction rate constants.

The EIS from the linearized model, as previously discussed, can be represented as a transfer function. This transfer function is of rational form with numerator and denominator which are polynomials in Laplace variable s. The highest degree of these polynomials in numerator and denominator depends on the number of state variables (reaction intermediates). In our current model, we have four state variables. This results in a rational polynomial in the denominator and numerator with a degree of four. Hence, we call this a fourth order transfer function.

Figure 2b shows that at potentials below 1.7 V, adsorbed OH (θ_{OH}) is the only intermediate species which is present. Hence, at these operating points, technically the fourth order transfer function can be approximated using a first order transfer function. In the following, an applied potential of 1.65 V is chosen to demonstrate model order reduction.

The model is simplified, i.e., the order is reduced, using singular value decomposition method and using only the information belonging to significant singular values. This model reduction algorithm is available in the MATLAB control system toolbox.[81] From the analysis, we found that at the potential of 1.65 V, the model order can be reduced to one. For comparing the fit, Bode plots are generated from both the nonlinear state-space model (Z_{sim}) and the first order model (Z_{red}) (Figure 3). The relative error between the full model and the reduced order model is in the order of 10^{-3} for both magnitude ($|Z|$) and phase (ϕ). These low values of relative error indicate that the impedance from the fourth order model at this voltage can be well approximated using a first order transfer function at an applied potential of 1.65 V.

The coefficients of this first order transfer function can be used for identifying the reaction rates involving the OH intermediates (θ_{OH}). However, an analytical expression of the first order transfer function involving these rates are necessary for the identification. In order to get this analytical expression, the model is linearized using θ_{OH} as the only adsorbed species. This gives

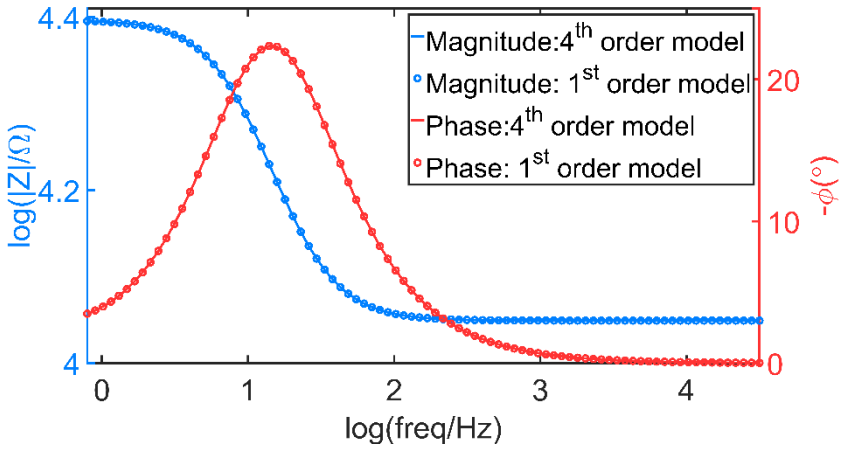

Figure 3. Bode plot at an applied potential of 1.65 V from first order approximate transfer function (reduced model) compared against the fourth order transfer function (full model). The relative errors are in the order of 10^{-3} for both magnitude and phase.

$$A = -U_{eq}\left(\overline{k_{f1}} + \overline{k_{f2}}\right)x_{OH} - \left(N_v\overline{k_{b1}}\right) \quad (36)$$

$$B = \frac{U_{eq}}{k_BT}\left(-\overline{k_{f2}}x_{OH}\theta_{\mathrm{OH}}^{eq} + \overline{k_{f1}}x_{OH}\left(1 - \theta_{OH}^{eq}\right)\right) \quad (37)$$

$$C = N_0q_e\left(-\overline{k_{b1}}N_v + \left(-\overline{k_{f1}} + \overline{k_{f2}}\right)U_{eq}x_{OH}\right) \quad (38)$$

$$D = \frac{U_{eq}N_0q_ex_{OH}}{k_BT}\left(\overline{k_{f1}}\left(1 - \theta_{\mathrm{OH}}^{eq}\right) + \overline{k_{f2}}\theta_{\mathrm{OH}}^{eq}\right) \quad (39)$$

The impedance of this system can then be expressed as a transfer function using eq. 34 - 35 and is obtained as

$$Z_{red}(s) = \frac{as + b}{cs + d} \quad (40)$$

where

$$a = \frac{U_{eq}N_0q_e}{k_BT}\left(\left(1 - \theta_{OH}^{eq}\right)x_{OH}\,\overline{k_{f1}} + \theta_{OH}^{eq}\,x_{OH}\,\overline{k_{f2}}\right) \quad (41)$$

$$b = \frac{2U_{eq}N_0\,q_e\,x_{OH}}{k_BT}\left(U_{eq}x_{OH}\left(\left(\theta_{OH}^{eq} - 1\right)\left(\overline{k_{f1}}\right)^2 - \theta_{OH}^{eq}\left(\overline{k_{f2}}\right)^2\right) - N_v\left(1 - \theta_{OH}^{eq}\right)\overline{k_{f1}}\,\overline{k_{b1}}\right) \quad (42)$$

$$c = 1 \quad (43)$$

$$d = \left(U_{eq}x_{OH}\left(\overline{k_{f1}} + \overline{k_{f2}}\right) + N_v\,\overline{k_{b1}}\right) \quad (44)$$

Thus, a first order transfer function (Z_{red}) is obtained for impedance at applied potential of 1.65 V, which consists of only three reaction rates $\overline{k_{f1}}, \overline{k_{f2}}$ and $\overline{k_{b1}}$ (eq. 40 - 44). By fitting this transfer function to experimental data at the same applied potential, the intrinsic reaction rates $\overline{k_{f1}}$, $\overline{k_{f2}}$ and $\overline{k_{b1}}$ can be identified directly from experimental measurements. For doing so, the fitting can be formulated as an optimization problem in which the reaction rates are varied until the simulated data matches the experimental data. The theoretically derived reaction rates from the DFT calculations and the Gerischer model can serve as starting values for this optimization. This fitting of the transfer function (eq. 40 - 44) in the complex plane is beyond the scope of this paper.

Model order reduction is advantageous when it comes to identification of rate constants because a transfer function of lower order has fewer rate constants and is therefore easier to identify. Furthermore, a parallel RC loop in an equivalent circuit also has a first order transfer function. Our analysis shows that the first order model gives a good fit at low potentials. This result validates the use of an RC parallel loop to represent charge transfer impedance at low potentials (1.2 - 1.7 V in this case). At higher potentials the order of transfer function is higher because of multiple intermediates and a single RC loop is insufficient at such potentials to represent the charge transfer impedance.

3.5 Simulation of extended EIS and comparison to experiment

As mentioned before, the experimentally measured EIS represents not only the charge transfer reactions at the interface, but additional contributions. Hence, in order to simulate an EIS similar to experiments, these other contributions also have to be included. In principle, these impedance contributions can be added to the nonlinear state-space approach as physical and chemical models. A stitching algorithm was recently suggested by Weddle et al.[82] for the

case of Li ion batteries. In the current study, we use a simple equivalent circuit model to include additional contributions (Figure 4).

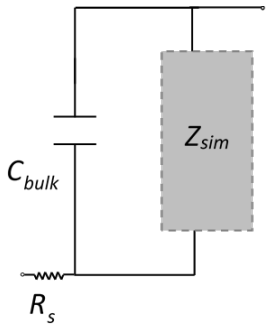

Figure 4 Equivalent circuit model of the hematite-water interface with impedance from the state-space model represented as Z_{sim}. R_S represents the series resistance and C_{bulk} represents the bulk capacitance.

The literature suggest different equivalent models for hematite.[83,84] The common part in these models is the series resistance R_S, and a bulk capacitance, C_{bulk}, in parallel with the impedance from the electrochemical interface. The interface impedance is generally represented by one or more R-RC loops either in series or parallel, attributed to different processes taking place at the interface. We replace these equivalent circuit elements with the impedance calculated from the linearized model (section 3.3.2) and call it Z_{sim}. To compare simulated EIS to experimental EIS, $R_s = 30\ \Omega$ and $C_{bulk} = 3\ \mu F$ are used, which are in agreement with values from the literature.[3,80] Both R_s and C_{bulk} are kept constant in the chosen applied potential range.

The EIS calculated using this model is shown in Figure 5. A potential range of 1.5 – 1.7 V and a frequency range of 0.1 Hz to 30 kHz are chosen. Experimental EIS for the same potentials and frequency range are also plotted. Experimental EIS was performed using a 3 electrode set-up with a Pt wire counter electrode and a Ag/AgCl reference electrode in a 1 M NaOH electrolyte solution as described in Sinha et al.[85] The measurements were carried out in a frequency range of 0.05 Hz to 300 KHz using a Biologic SP-150 potentiostat. The magnitude

of the modulation signal applied to the potential was 10 mV. The potential at which the EIS scans were performed was increased step-wise by 23 mV between 1 V and 1.7 V versus RHE.

The Nyquist representation of both simulated and experimental EIS are shown in Figure 5a. It can be seen that the model calculates the impedance arcs and features similar to the experiments. In order to get a clear comparison of the frequency response, Bode plot of the same data are shown in Figure 5b. It is seen that the magnitudes of impedance and its variation over different potentials(blue curves) and frequency are captured well by the model. Likewise, in the phase plot (red curves), the frequencies corresponding to the position of the peaks from the simulated plots are in good agreement with the corresponding experimental curves. The only minor difference observed between the experimental and simulated data is the depressed

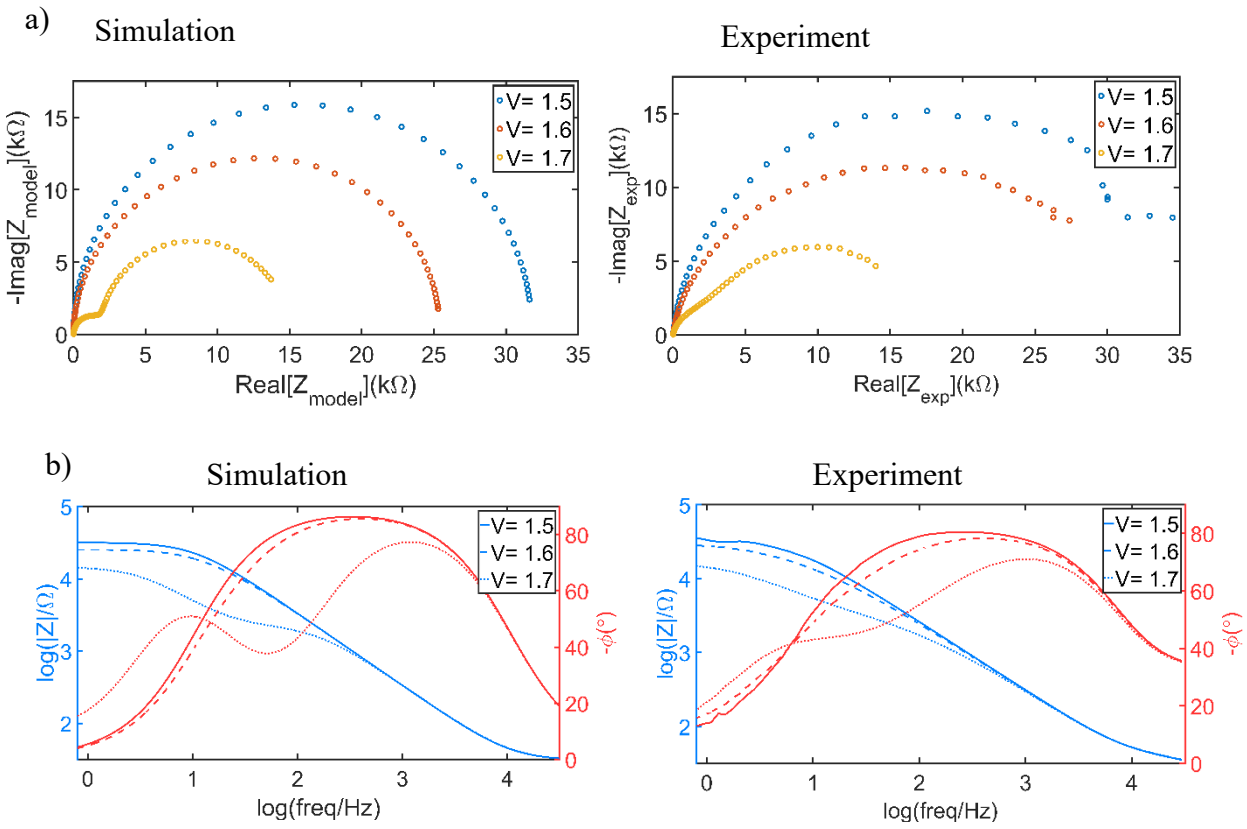

Figure 5. (a) Nyquist plots of impedance spectra from the simulation at potentials 1.5 V, 1.6 V and 1.7 V compared against experimental EIS at same potentials. (b) Comparison between Bode representations of the same data showing the variation of absolute value of impedance and phase angle against frequency of perturbation between 0.1 Hz and 30 kHz.

semi-circles in the experimental Nyquist plot and the concomitant spread of the curve in the Bode phase plot due to the electrochemical heterogeneity of the measured hematite surface[86] as compared to the ideal (110) surface assumed in the model. Since the added RC component values are kept constant, all the variations in the simulated plots at different potentials are due to the impedance from the electrochemical model (Z_{sim}).

The fact that the model can calculate impedance spectra similar to experiment, with the applied voltage as the only variable input, is remarkable. It implies that the electrochemical interface data at any operating potential can be simulated with the model. Such a continuous nonlinear description of an electrochemical system cannot be achieved by using traditional equivalent circuit analysis, as it defines the system at discrete operating potentials. Thus the developed nonlinear state-space approach in this study captures the actual chemistry and gives a continuous non-linear description of the system which is a milestone in the analysis of electrochemical data.

4. Summary and Outlook

We have developed a new approach to calculate electrochemical data directly from multistep reactions. The feasibility of the method is proven with a case study on a typical interface in a photo-electrochemical cell, the α-Fe_2O_3 - electrolyte interface. Using the developed state-space model, the current–voltage characteristics and electrochemical impedance spectra were simulated. These two are also the main plots which are experimentally measured in order to investigate such interfaces. The advantage of this approach is that 1) the electrochemical data is fully simulated from an electrochemical model (no equivalent circuits, no experimental input); 2) the data can be directly related to the underlying electrochemistry as it is simulated from an electrochemical model; 3) the model can simulate the coverage of OER intermediates at the surface sites at different operating potentials; this data is extremely challenging to obtain

experimentally.; 4) the model is modular, such that other chemical and physical processes like diffusion and illumination, can be added as well. Due to the generic nature of our approach, it can be applied on different materials straightforwardly. Also, the impact of different reaction mechanisms and parameters for different materials can be studied quickly and easily.

As an outlook, we propose to integrate simulations and experiments for identifying reaction rates. To do this, our model which currently considers only charge transfer reactions, needs to be extended to represent the entire electrochemical interface. A first step towards this is already explained in section 3.5 where the developed state-space model is added as a circuit component in a typical equivalent circuit model of an electrochemical interface in water splitting. These equivalent circuit elements need to be replaced by physical and chemical models which are integrated into the state-space model. Possibly, additional contributions to the electrochemical interface are required as well. In a second step, the entire model can be optimized for the reaction rates by fitting to experimental data. The theoretical reaction rates, currently calculated by DFT and Gerischer model, serve as best starting values for the optimization. The reaction rates which are obtained after this optimization will be more realistic than the theoretical derived ones as they are derived from a real system (optimization with experimental data from solid-liquid interface). Thus, the reaction rates for intermediate reactions can be derived by using this method. This will facilitate the identification of rate limiting processes at semiconductor-electrolyte interfaces in a new manner and unprecedentedly close to real systems under operation.

AUTHOR INFORMATION

Corresponding Author

* Email: a.bieberle@differ.nl

[§]Vrije Universiteit Brussel (VUB), Fundamental Electricity and Instrumentation, Pleinlaan 2, 1050 Brussels, Belgium.

[‖] Eindhoven University of Technology, Mechanical Engineering, Control Systems Technology, PO Box 513, 5600 MB Eindhoven, The Netherlands.

Author Contributions

The manuscript was written through contributions of all authors. All authors have given approval to the final version of the manuscript.

Notes

The authors declare no competing financial interest

ACKNOWLEDGMENT

George acknowledge funding from the Shell-NWO/FOM "Computational Sciences for Energy Research" PhD program (CSER-PhD; nr. i32; project number 15CSER021). Zhang and Bieberle-Hütter acknowledge the financial support from NWO (FOM program nr. 147 "CO2 neutral fuels") and from M-ERA.NET (project "MuMo4PEC" with project number M-ERA.NET 4089). Supercomputing facilities of the Dutch national supercomputers SURFsara/Lisa and Cartesius are acknowledged. Van Berkel acknowledges that this work has been carried out within the framework of the EUROfusion Consortium and has received funding from the Euratom research and training programme 2014-2018 under grant agreement No 633053. The views and opinions expressed herein do not necessarily reflect those of the European Commission. The fruitful discussions with researchers from the ELEC department of Vrije Universiteit Brussels, especially with prof. dr. ir. Gerd Vandersteen, are acknowledged. Dr. Aafke Bronneberg is gratefully acknowledged for reading the manuscript and giving valuable comments.

ABBREVIATIONS

OER, oxygen evolution reaction; PEC, photoelectrochemical cell; DFT, density functional theory; ORR, oxygen reduction reaction; EIS, electrochemical impedance spectra.

REFERENCES

(1) Lewis, N. S.; Nocera, D. G. Powering the Planet: Chemical Challenges in Solar Energy Utilization. *Proc. Natl. Acad. Sci.* **2006**, *103*, 15729–15735.

(2) van de Krol, R. Principles of Photoelectrochemical Cells. In *Photoelectrochemical Hydrogen Production*; van de Krol, R., Grätzel, M., Eds.; Springer US: Boston, MA, **2012**, 13–67.

(3) Lopes, T.; Andrade, L.; Ribeiro, H. A.; Mendes, A. Characterization of Photoelectrochemical Cells for Water Splitting by Electrochemical Impedance Spectroscopy. *Int. J. Hydrogen Energy* **2010**, *35*, 11601–11608.

(4) Andrade, L.; Lopes, T.; Ribeiro, H. A.; Mendes, A. Transient Phenomenological Modeling of Photoelectrochemical Cells for Water Splitting - Application to Undoped Hematite Electrodes. *Int. J. Hydrogen Energy* **2011**, *36*, 175–188.

(5) Fujishima, A.; Honda, K. Electrochemical Photolysis of Water at a Semiconductor Electrode. *Nature* **1972**, *238*, 37–38.

(6) Sivula, K.; Le Formal, F.; Grätzel, M. Solar Water Splitting: Progress Using Hematite (α-Fe 2O3) Photoelectrodes. *ChemSusChem* **2011**, *4*, 432–449.

(7) Bignozzi, C. A.; Caramori, S.; Cristino, V.; Argazzi, R.; Meda, L.; Tacca, A. Nanostructured Photoelectrodes Based on WO_3: Applications to Photooxidation of Aqueous Electrolytes. *Chem. Soc. Rev.* **2013**, *42*, 2228–2246.

(8) Liang, Y.; Tsubota, T.; Mooij, L. P. A.; Van De Krol, R. Highly Improved Quantum Efficiencies for Thin Film BiVO4 Photoanodes. *J. Phys. Chem. C* **2011**, *115*, 17594–17598.

(9) Zhang, X.; Cao, C.; Bieberle-Hütter, A. Orientation Sensitivity of Oxygen Evolution Reaction on Hematite. *J. Phys. Chem. C* **2016**, *120*, 28694–28700.

(10) van de Krol, R. Photoelectrochemical Measurements. In *Photoelectrochemical Hydrogen Production*; van de Krol, R., Grätzel, M., Eds.; Springer US: Boston, MA, **2012**, 69–117.

(11) Zhang, X.; Klaver, P.; Van Santen, R.; Van De Sanden, M. C. M.; Bieberle-Hütter, A. Oxygen Evolution at Hematite Surfaces: The Impact of Structure and Oxygen Vacancies on Lowering the Overpotential. *J. Phys. Chem. C* **2016**, *120*, 18201–18208.

(12) Liao, P.; Keith, J. A.; Carter, E. A. Water Oxidation on Pure and Doped Hematite (0001) Surfaces: Prediction of Co and Ni as Effective Dopants for Electrocatalysis. *J. Am. Chem. Soc.* **2012**, *134*, 13296–13309.

(13) Rossmeisl, J.; Qu, Z. W.; Zhu, H.; Kroes, G. J.; Nørskov, J. K. Electrolysis of Water on Oxide Surfaces. *J. Electroanal. Chem.* **2007**, *607*, 83–89.

(14) Zhang, X.; Klaver, P.; Van Santen, R.; Van De Sanden, M. C. M.; Bieberle-Hütter, A. Oxygen Evolution at Hematite Surfaces: The Impact of Structure and Oxygen Vacancies on Lowering the Overpotential. *J. Phys. Chem. C* **2016**, *120*, 18201–18208.

(15) Toroker, M. C. Theoretical Insights into the Mechanism of Water Oxidation on Nonstoichiometric and Titanium-Doped Fe $_2$ O $_3$ (0001). *J. Phys. Chem. C* **2014**, *118*, 23162–23167.

(16) Man, I. C.; Su, H. Y.; Calle-Vallejo, F.; Hansen, H. A.; Martínez, J. I.; Inoglu, N. G.; Kitchin, J.; Jaramillo, T. F.; Nørskov, J. K.; Rossmeisl, J. Universality in Oxygen Evolution Electrocatalysis on Oxide Surfaces. *ChemCatChem* **2011**, *3*, 1159–1165.

(17) Toroker, M. C.; Kanan, D. K.; Alidoust, N.; Isseroff, L. Y.; Liao, P.; Carter, E. A. First Principles Scheme to Evaluate Band Edge Positions in Potential Transition Metal Oxide Photocatalysts and Photoelectrodes. *Phys. Chem. Chem. Phys.* **2011**, *13*, 16644.

(18) Liao, P.; Carter, E. A. New Concepts and Modeling Strategies to Design and Evaluate Photo-Electro-Catalysts Based on Transition Metal Oxides. *Chem. Soc. Rev.* **2013**, *42*, 2401–2422.

(19) Frydendal, R.; Busch, M.; Halck, N. B.; Paoli, E. A.; Krtil, P.; Chorkendorff, I.; Rossmeisl, J. Enhancing Activity for the Oxygen Evolution Reaction: The Beneficial Interaction of Gold with Manganese and Cobalt Oxides. *ChemCatChem* **2015**, *7*, 149–154.

(20) Ovcharenko, R.; Voloshina, E.; Sauer, J. Water Adsorption and O-Defect Formation on Fe_2O_3 (0001) Surfaces. *Phys. Chem. Chem. Phys.* **2016**, *3*, 25560–25568.

(21) Tkalych, A. J.; Zhuang, H. L.; Carter, E. A. A Density Functional + U Assessment of Oxygen Evolution Reaction Mechanisms on β-NiOOH. *ACS Catal.* **2017**, *7*, 5329–5339.

(22) Kerisit, S.; Cooke, D. J.; Spagnoli, D.; Parker, S. C. Molecular Dynamics Simulations of the Interactions between Water and Inorganic Solids. *J. Mater. Chem.* **2005**, *15*, 1454.

(23) Von Rudorff, G. F.; Jakobsen, R.; Rosso, K. M.; Blumberger, J. Fast Interconversion of Hydrogen Bonding at the Hematite (001)-Liquid Water Interface. *J. Phys. Chem. Lett.* **2016**, *7*, 1155–1160.

(24) Pham, T. A.; Ping, Y.; Galli, G. Modelling Heterogeneous Interfaces for Solar Water Splitting. *Nat. Mater.* **2017**, *16*, 401–408.

(25) Zhang, X.; Bieberle-Hütter, A. Modeling and Simulations in Photoelectrochemical Water Oxidation: From Single Level to Multiscale Modeling. *ChemSusChem* **2016**, *9*, 1223–1242.

(26) Lasia, A. Definition of Impedance and Impedance of Electrical Circuits. In *Electrochemical Impedance Spectroscopy and its Applications*; Springer New York: New York, NY, **2014**, 7–66.

(27) Zheltikov, A. Impedance Spectroscopy: Theory, Experiment, and Applications Second

Edition. Evgenij Barsoukov and J. Ross Macdonald (Eds). John Wiley & Sons, Inc., Hoboken, New Jersey, 2005, Pp. 595. *J. Raman Spectrosc. 38*, 122.

(28) Macdonald, J. R.; Johnson, W. B. Fundamentals of Impedance Spectroscopy. In *Impedance Spectroscopy*; John Wiley & Sons, Ltd, **2005**, 1–26.

(29) Bertoluzzi, L.; Lopez-Varo, P.; Jiménez Tejada, J. A.; Bisquert, J. Charge Transfer Processes at the Semiconductor/Electrolyte Interface for Solar Fuel Production: Insight from Impedance Spectroscopy. *J. Mater. Chem. A* **2016**, *4*, 2873–2879.

(30) Bertoluzzi, L.; Bisquert, J. Equivalent Circuit of Electrons and Holes in Thin Semiconductor Films for Photoelectrochemical Water Splitting Applications. *J. Phys. Chem. Lett.* **2012**, *3*, 2517–2522.

(31) Mora-Seró, I.; Villarreal, T. L.; Bisquert, J.; Pitarch, Á.; Gómez, R.; Salvador, P. Photoelectrochemical Behavior of Nanostructured TiO2 Thin-Film Electrodes in Contact with Aqueous Electrolytes Containing Dissolved Pollutants: A Model for Distinguishing between Direct and Indirect Interfacial Hole Transfer from Photocurrent Measurements. *J. Phys. Chem. B* **2005**, *109*, 3371–3380.

(32) Liu, H.; Li, X. Z.; Leng, Y. J.; Li, W. Z. An Alternative Approach to Ascertain the Rate-Determining Steps of TiO 2 Photoelectrocatalytic Reaction by Electrochemical Impedance Spectroscopy. *J. Phys. Chem. B* **2003**, *107*, 8988–8996.

(33) Haussener, S.; Xiang, C.; Spurgeon, J. M.; Ardo, S.; Lewis, N. S.; Weber, A. Z. Modeling, Simulation, and Design Criteria for Photoelectrochemical Water-Splitting Systems. *Energy Environ. Sci.* **2012**, *5*, 9922–9935.

(34) Kemppainen, E.; Halme, J.; Lund, P. Physical Modeling of Photoelectrochemical Hydrogen Production Devices. *J. Phys. Chem. C* **2015**, *119*, 21747–21766.

(35) He, Y.; Gamba, I. M.; Lee, H. C.; Ren, K. On the Modeling and Simulation of Reaction-Transfer Dynamics in Semiconductor-Electrolyte Solar Cells. *Siam J. Appl. Math.* **2015**,

75, 2515–2539.

(36) Harmon, M.; Gamba, I. M.; Ren, K. Numerical Algorithms Based on Galerkin Methods for the Modeling of Reactive Interfaces in Photoelectrochemical (PEC) Solar Cells. *J. Comput. Phys.* **2016**, *327*, 140–167.

(37) Andrade, L.; Lopes, T.; Mendes, A. Dynamic Phenomenological Modeling of PEC Cells for Water Splitting under Outdoor Conditions. *Energy Procedia* **2011**, *22*, 23–34.

(38) Tang, J.; Durrant, J. R.; Klug, D. R. Mechanism of Photocatalytic Water Splitting in TiO2. Reaction of Water with Photoholes, Importance of Charge Carrier Dynamics, and Evidence for Four-Hole Chemistry. *J. Am. Chem. Soc.* **2008**, *130*, 13885–13891.

(39) Zandi, O.; Hamann, T. W. Determination of Photoelectrochemical Water Oxidation Intermediates on Haematite Electrode Surfaces Using Operando Infrared Spectroscopy. *Nat. Chem.* **2016**, *8*, 778–783.

(40) Zhang, M.; de Respinis, M.; Frei, H. Time-Resolved Observations of Water Oxidation Intermediates on a Cobalt Oxide Nanoparticle Catalyst. *Nat. Chem.* **2014**, *6*, 362–367.

(41) Doan, H. Q.; Pollock, K. L.; Cuk, T. Transient Optical Diffraction of GaN/Aqueous Interfaces: Interfacial Carrier Mobility Dependence on Surface Reactivity. *Chem. Phys. Lett.* **2016**, *649*, 1–7.

(42) Rossmeisl, J.; Logadottir, A.; Nørskov, J. K. Electrolysis of Water on (Oxidized) Metal Surfaces. *Chem. Phys.* **2005**, *319*, 178–184.

(43) Davis, M. E.; J., D. R. Microkinetic Analysis of Catalytic Reactions. *Fundam. Chem. React. Eng.* **1993**, *217*, 240–259.

(44) De Morais, R. F.; Sautet, P.; Loffreda, D.; Franco, A. A. A Multiscale Theoretical Methodology for the Calculation of Electrochemical Observables from Ab Initio Data: Application to the Oxygen Reduction Reaction in a Pt(1 1 1)-Based Polymer Electrolyte Membrane Fuel Cell. *Electrochim. Acta* **2011**, *56*, 10842–10856.

(45) Exner, K. S.; Sohrabnejad-Eskan, I.; Over, H. A Universal Approach to Determine the Free Energy Diagram of an Electrocatalytic Reaction. *ACS Catal.* **2018**, *8*, 1864–1879.

(46) Rüdiger, M. Electron Transfer Theories. In *Semiconductor Electrochemistry*; Wiley-Blackwell, **2015**, 127–168.

(47) https://nl.mathworks.com/discovery/state-space.html 2019.

(48) Friedland, B. *Control System Design: An Introduction to State-Space Methods (Dover Books on Engineering)*; Dover Publications, Incorporated, 2005.

(49) Hansen, H. A.; Viswanathan, V.; Nørskov, J. K. Unifying Kinetic and Thermodynamic Analysis of 2 e $^-$ and 4 e $^-$ Reduction of Oxygen on Metal Surfaces. *J. Phys. Chem. C* **2014**, *118*, 6706–6718.

(50) Mitterdorfer, A.; Gauckler, L. J. Reaction Kinetics of the Pt, O2(g)|c-ZrO2 System: Precursor-Mediated Adsorption. *Solid State Ionics* **1999**, *120*, 211–225.

(51) Bieberle, A.; Gauckler, L. J. State-Space Modeling of the Anodic SOFC System Ni, H2-H2O|YSZ. *Solid State Ionics* **2002**, *146*, 23–41.

(52) García-Osorio, D. A.; Jaimes, R.; Vazquez-Arenas, J.; Lara, R. H.; Alvarez-Ramirez, J. The Kinetic Parameters of the Oxygen Evolution Reaction (OER) Calculated on Inactive Anodes via EIS Transfer Functions: $^{\bullet}$OH Formation. *J. Electrochem. Soc.* **2017**, *164*, E3321–E3328.

(53) Tourwé, E.; Breugelmans, T.; Pintelon, R.; Hubin, A. Extraction of a Quantitative Reaction Mechanism from Linear Sweep Voltammograms Obtained on a Rotating Disk Electrode. *WIT Trans. Eng. Sci.* **2007**, *54*, 173–182.

(54) Holm, T.; Harrington, D. A. Understanding Reaction Mechanisms Using Dynamic Electrochemical Impedance Spectroscopy: Modeling of Cyclic Voltammetry and Impedance Spectra. *ECS Trans.* **2018**, *85*, 167–176.

(55) van de Krol, R.; Liang, Y.; Schoonman, J. Solar Hydrogen Production with

Nanostructured Metal Oxides. *J. Mater. Chem.* **2008**, *18*, 2311.

(56) Hellman, A.; Iandolo, B.; Wickman, B.; Grönbeck, H.; Baltrusaitis, J. Electro-Oxidation of Water on Hematite: Effects of Surface Termination and Oxygen Vacancies Investigated by First-Principles. *Surf. Sci.* **2015**, *640*, 45–49.

(57) Marcus, R. A.; Sutin, N. Electron Transfers in Chemisrty and Biology. *Biochim. Biophys. Acta* **1985**, *811*, 265.

(58) Gerischer, H. Electron-Transfer Kinetics of Redox Reactions at the Semiconductor/Electrolyte Contact. A New Approach. *J. Phys. Chem.* **1991**, *95*, 1356–1359.

(59) Peter, L. M. Energetics and Kinetics of Light-Driven Oxygen Evolution at Semiconductor Electrodes: The Example of Hematite. *J. Solid State Electrochem.* **2013**, *17*, 315–326.

(60) Mitterdorfer, A. Identification of the Reaction Mechanism of the Pt, O2(g)|yttria-Stabilized Zirconia System Part II: Model Implementation, Parameter Estimation, and Validation. *Solid State Ionics* **1999**, *117*, 203–217.

(61) Rüdiger, M. Charge Transfer Processes at the Semiconductor–Liquid Interface. In *Semiconductor Electrochemistry*; Wiley-Blackwell, **2015**, 169–266.

(62) Gerischer, H. Charge Transfer Processes at Semiconductor-Electrolyte Interfaces in Connection with Problems of Catalysis. *Surf. Sci.* **1969**, *18*, 97–122.

(63) Krishtalik, L. I. PH-Dependent Redox Potential: How to Use It Correctly in the Activation Energy Analysis. *Biochim. Biophys. Acta* **2003**, *1604*, 13–21.

(64) Khalil, H. K. *Nonlinear Systems*; Pearson Education; Prentice Hall, **2002**.

(65) Mitterdorfer, A. Identification of the Reaction Mechanism of the Pt, O2(g)|yttria-Stabilized Zirconia System Part I: General Framework, Modelling, and Structural Investigation. *Solid State Ionics* **1999**, *117*, 187–202.

(66) Matlab Simulink Release 2016a. The MathWorks: Natick, MA, USA.

(67) Pintelon, R.; Schoukens, J. *System Identification:A Frequency Domain Approach*; John Wiley & Sons, Inc., **2012**.

(68) Tamirat, A. G.; Rick, J.; Dubale, A. A.; Su, W.-N.; Hwang, B.-J. Using Hematite for Photoelectrochemical Water Splitting: A Review of Current Progress and Challenges. *Nanoscale Horiz.* **2016**, *1*, 243–267.

(69) Nellist, M. R.; Laskowski, F. A. L.; Lin, F.; Mills, T. J.; Boettcher, S. W. Semiconductor-Electrocatalyst Interfaces: Theory, Experiment, and Applications in Photoelectrochemical Water Splitting. *Acc. Chem. Res.* **2016**, *49*, 733–740.

(70) Sivula, K.; van de Krol, R. Semiconducting Materials for Photoelectrochemical Energy Conversion. *Nat. Rev. Mater.* **2016**, *1*, 15010.

(71) Mishra, M.; Chun, D.-M. α-Fe2O3 as a Photocatalytic Material: A Review. *Appl. Catal. A Gen.* **2015**, *498*, 126–141.

(72) Kment, S.; Schmuki, P.; Hubicka, Z.; Machala, L.; Kirchgeorg, R.; Liu, N.; Wang, L.; Lee, K.; Olejnicek, J.; Cada, M.; et al. Photoanodes with Fully Controllable Texture: The Enhanced Water Splitting Efficiency of Thin Hematite Films Exhibiting Solely (110) Crystal Orientation. *ACS Nano* **2015**, *9*, 7113–7123.

(73) Iandolo, B.; Hellman, A. The Role of Surface States in the Oxygen Evolution Reaction on Hematite. *Angew. Chemie* **2014**, *126*, 13622–13626.

(74) Klahr, B.; Gimenez, S.; Fabregat-Santiago, F.; Hamann, T.; Bisquert, J. Water Oxidation at Hematite Photoelectrodes: The Role of Surface States. *J. Am. Chem. Soc.* **2012**, *134*, 4294–4302.

(75) Lewis, N. S. Progress in Understanding Electron-Transfer Reactions at Semiconductor/Liquid Interfaces. *J. Phys. Chem. B* **1998**, *102*, 4843–4855.

(76) Cendula, P.; Tilley, S. D.; Gimenez, S.; Bisquert, J.; Schmid, M.; Grätzel, M.;

Schumacher, J. O. Calculation of the Energy Band Diagram of a Photoelectrochemical Water Splitting Cell. *J. Phys. Chem. C* **2014**, *118*, 29599–29607.

(77) Heidaripour, A.; Ajami, N.; Miandari, S. Research of Gerischer Model in Transferring Electrons between Energy States of CdS Thin Film and Ferro-Ferric Redox System. **2015**, *3*, 59–64.

(78) Hankin, A.; Alexander, J. C.; Kelsall, G. H. Constraints to the Flat Band Potential of Hematite Photo-Electrodes. *Phys. Chem. Chem. Phys.* **2014**, *16*, 16176–16186.

(79) Gaudy, Y. K.; Haussener, S.; Sivula, K.; Modestino, M. A.; Haussener, S.; Jacobsson, T. J.; Fjällström, V.; Edoff, M.; Edvinsson, T.; Walter, M. G.; et al. Utilizing Modeling, Experiments, and Statistics for the Analysis of Water-Splitting Photoelectrodes. *J. Mater. Chem. A* **2016**, *4*, 3100–3114.

(80) Steier, L.; Herraiz-Cardona, I.; Gimenez, S.; Fabregat-Santiago, F.; Bisquert, J.; Tilley, S. D.; Grätzel, M. Understanding the Role of Underlayers and Overlayers in Thin Film Hematite Photoanodes. *Adv. Funct. Mater.* **2014**, *24*, 7681–7688.

(81) Hamnett, A. Chapter 2 Semiconductor Electrochemistry. In *Electrode Kinetics: Reactions*; Compton, R. G., Ed.; Comprehensive Chemical Kinetics; Elsevier, **1988**, 61–246.

(82) Weddle, P. J.; Kee, R. J.; Vincent, T. A Stitching Algorithm to Identify Wide-Bandwidth Electrochemical Impedance Spectra for Li-Ion Batteries Using Binary Perturbations. *J. Electrochem. Soc.* **2018**, *165*, A1679–A1684.

(83) Klahr, B.; Gimenez, S.; Fabregat-Santiago, F.; Bisquert, J.; Hamann, T. W. Electrochemical and Photoelectrochemical Investigation of Water Oxidation with Hematite Electrodes. *Energy Environ. Sci.* **2012**, *5*, 7626.

(84) Le Formal, F.; Pendlebury, S. R.; Cornuz, M.; Tilley, S. D.; Grätzel, M.; Durrant, J. R. Back Electron-Hole Recombination in Hematite Photoanodes for Water Splitting. *J. Am.*

Chem. Soc. **2014**, *136*, 2564–2574.

(85) Sinha, R.; Tanyeli, İ.; Lavrijsen, R.; van de Sanden, M. C. M.; Bieberle-Hütter, A. The Electrochemistry of Iron Oxide Thin Films Nanostructured by High Ion Flux Plasma Exposure. *Electrochim. Acta* **2017**, *258*, 709–717.

(86) Lucas, M.; Boily, J.-F. Mapping Electrochemical Heterogeneity at Iron Oxide Surfaces: A Local Electrochemical Impedance Study. *Langmuir* **2015**, *31*, 13618–13624.

Table of Contents (TOC) Image